International Journal of Nanomedicine

Dovepress
Taylor & Francis Group

Open Access Full Text Article

ORIGINAL RESEARCH

# Ru Complex-Functionalized Au Nanospheres for Suppressing Tumor Growth and Metastasis: Photothermal Therapy Combined with Chemotherapy Using Nanoplatforms

Di Zhu[1], Bo Hu[2,3], Lan Zhang[1], Dan Gao[1], Mengyue Ni[2,3], Yu Lu[2,3], Yuji Wang[2,3]

[1]Department of Pharmacy, Xuanwu Hospital of Capital Medical University, Beijing, 100053, People's Republic of China; [2]Department of Medicinal Chemistry, College of Pharmaceutical Sciences of Capital Medical University, Beijing, 100069, People's Republic of China; [3]Beijing Key Laboratory of Drug Innovation for Neuro-Oncology, Beijing Engineering Research Center of Targeted Drugs and Cell Therapy for CNS Tumors, Beijing, 100069, People's Republic of China

Correspondence: Yu Lu; Yuji Wang, Department of Medicinal Chemistry, College of Pharmaceutical Sciences of Capital Medical University, Beijing, 100069, People's Republic of China, Email luyu@mail.ccmu.edu.cn; wangyuji@ccmu.edu.cn



**Background:** The clinical translation of ruthenium complexes as alternatives to platinum-based drugs is hindered by insufficient tumor targeting and limited therapeutic efficacy. Although nanodrug delivery systems (NDDS) offer potential solutions, existing Ru platforms often fail to integrate multi-modal therapeutic mechanisms effectively. This study aimed to construct a tumor-targeted Ru–Au nanoplatform, KKS-Ru@AuNPs, that synergizes Ru-based chemotherapy with photothermal therapy (PTT) to suppress tumor growth and metastasis simultaneously.

**Methods:** The KKS-Ru@AuNPs system was developed by conjugating arginine-glycine-aspartic acid peptide-modified Ru complexes with Au nanospheres. The nanoscale properties of KKS-Ru@AuNPs were characterized utilizing transmission electron microscopy and nanoparticle size-measuring techniques. The photothermal performance of the KKS-Ru@AuNP system was assessed using near-infrared irradiation assays utilizing an infrared thermal imaging device. Additionally, anti-tumor efficacy was evaluated in an A549 xenograft mouse model, and tumor-targeting efficiency was quantified by inductively coupled plasma mass spectrometry (ICP-MS).

**Results:** The KKS-Ru@AuNPs exhibited nanospherical morphology, with nanospheres having a diameter of ~75 nm. Compared with AuNPs, KKS-Ru@AuNPs exhibited enhanced stability and superior photothermal conversion efficiency. Under in vitro conditions with irradiation using an 808 nm laser, the KKS-Ru@AuNPs exhibited significantly enhanced cytotoxic effects. In vivo studies revealed that KKS-Ru@AuNPs achieve greater tumor accumulation than that achieved by AuNPs. The synergistic therapeutic effect of KKS-Ru@AuNPs was evidenced by an 84.6% reduction in tumor weight and a 46% decrease in the number of lung metastatic nodules.

**Conclusion:** This study established a Ru-based NDDS by integrating active targeting, chemotherapy, and PTT into a single platform, overcoming the limitations of conventional monotherapeutic approaches. However, challenges persist in terms of long-term biosafety due to hepatic Au accumulation and tumor heterogeneity-dependent targeting efficiency. Future studies should focus on degradable carrier designs and multi-omics mechanistic analysis to promote clinical applicability of Ru-based NDDSs.

**Keywords:** Ru complexes, Au nanoparticles, photothermal therapy, tumor suppression, anti-metastasis

## Introduction

In recent years, ruthenium complexes have garnered significant attention as promising alternatives to platinum-based drugs.[1–3] Unlike traditional chemotherapeutic agents, Ru complexes exhibit not only reduced systemic toxicity and more favorable safety profiles, but also distinctive redox activities,[4] multi-target mechanisms of action,[5] and excellent biocompatibility.[6] Ru complexes exert antitumor effects by disrupting the cancer cell cycle and inducing the apoptotic signaling pathways. Nonetheless, small-molecule Ru complexes encounter substantial challenges in clinical translation.[7]

Received: 17 June 2025
Accepted: 11 October 2025
Published: 21 October 2025

**Graphical Abstract**

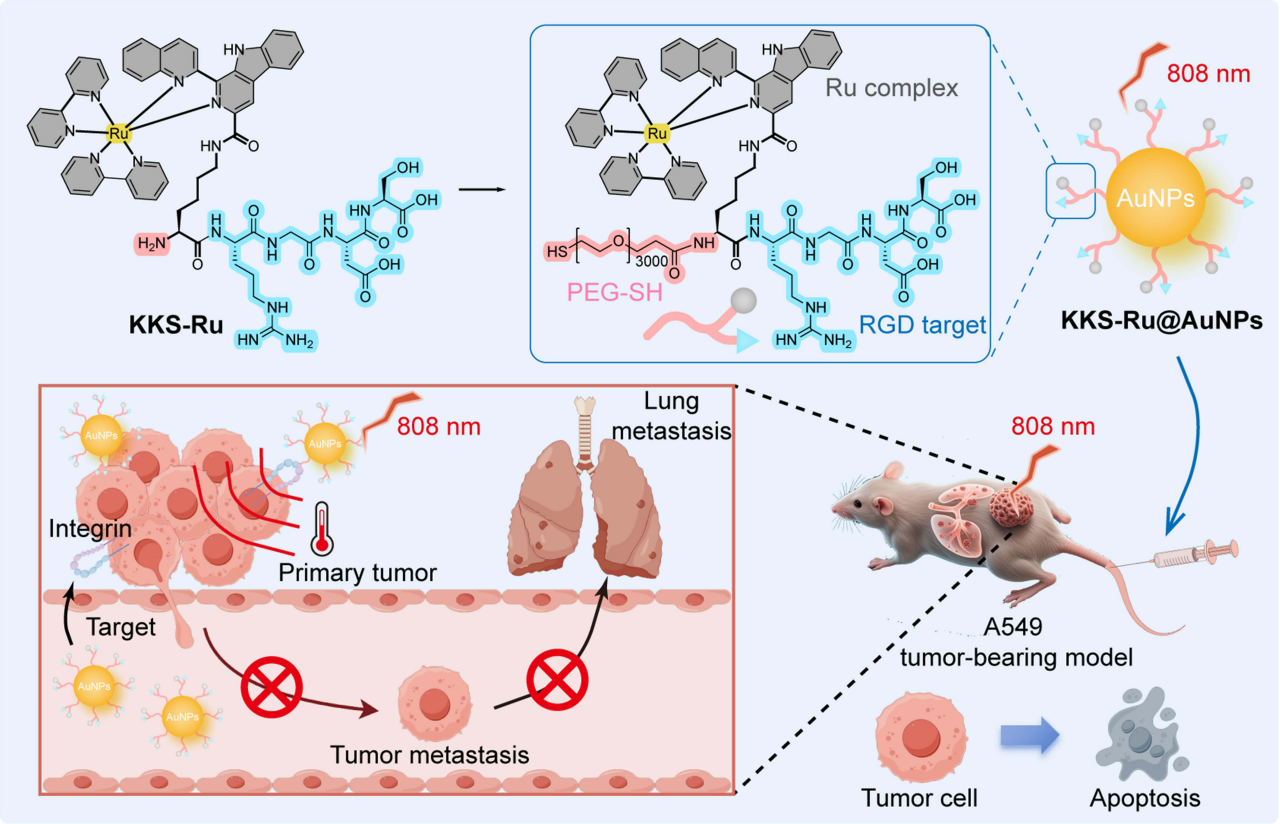


Firstly, the rapid metabolism and inadequate tumor targeting significantly reduce the accumulation efficiency of Ru complexes in vivo.[8,9] Secondly, the reliance of Ru complexes on a single chemotherapeutic mechanism is often insufficient to effectively inhibit tumor metastasis and angiogenesis.[10–12] Although structural optimization can address certain pharmacokinetic limitations of Ru complexes, achieving a balance between the steric hindrance of ligands and requisite lipophilicity remains challenging.[7,13–16] To address the challenges and limitations associated with the use of Ru complexes, nanodrug delivery systems (NDDSs) have been developed.[17–20] NDDSs present innovative approaches for the functional enhancement of Ru-based therapeutics.[21–23]

Recently, gold nanoparticles (AuNPs) have emerged as exemplary drug delivery platforms owing to their distinctive surface plasmon resonance properties, tunable photothermal conversion capabilities, and biocompatibility.[24] Utilizing advanced surface functionalization techniques,[25] AuNPs can achieve passive targeting via enhanced permeability and retention (EPR) effect[26] and active targeting via ligand modification.[9,27] Surface functionalization of AuNPs substantially increases drug accumulation at tumor sites.[28] Furthermore, the multifunctional integration capabilities of NDDS facilitate the incorporation of photothermal therapy, chemotherapy, and antimetastatic functions into a single platform, overcoming the limitations associated with traditional monotherapeutic approaches.[29] Recent studies have reported that Ru (η6-p-cymene) complexes co-modified with poly(*N*-vinylpyrrolidone) on AuNPs (Ru@AuNPs) can markedly enhance the cytotoxic efficacy against colorectal cancer cells by improving cell membrane permeability, facilitating the development of multimodal therapeutic.[25] In 2021, peptidyl arginine deiminase 4 (PAD4) inhibitor-loaded Au nanorods were reported to demonstrate superior tumor suppression and antimetastatic activities compared with those of PAD4 inhibitor-

loaded Au nanospheres. The improved tumor suppression and antimetastatic activities observed using PAD4 inhibitor-loaded Au nanorods can be attributed to increased cellular and tissue permeability.[30]

Previous studies have explored hybrid Ru–Au systems; for example, Ru($\eta^6$-*p*-cymene) complexes co-modified with poly(*N*-vinylpyrrolidone) on AuNPs were shown to enhance cytotoxicity against colorectal cancer cells by improving membrane permeability.[25] In another study, PAD4 inhibitor-loaded Au nanorods outperformed nanospheres in tumor suppression and antimetastatic activity, attributed to improved tissue permeability.[30] However, these systems often lack specific targeting ligands and exhibit limited spatial-temporal synergy between therapeutic components.

This study focused on developing a Ru-Au nanocarrier system (KKS-Ru@AuNPs), designed to overcome these limitations. This system preserves the photothermal properties AuNPs while enhancing Au accumulation in tumors by incorporating Ru complexes to achieve dual antitumor and antimetastatic effects. The developed nanocarrier system utilized AuNPs as core carriers with near-infrared photothermal conversion capability for physical ablation. The KKS-Ru complex, which has integrin-targeting properties, was incorporated with AuNPs to form KKS-Ru@AuNPs. The presence of an arginine-glycine-aspartic acid sequence (RGDS)-targeting moiety in KKS-Ru@AuNPs allowed detection of overexpressed integrin receptors in tumor cells, synergistically augmenting tumor accumulation and enhancing antimetastatic efficacy of the nanoparticles. The KKS-Ru@AuNPs maintained a photothermal conversion efficiency comparable to that of unmodified AuNPs in vitro, enhancing tumoricidal activity. Additionally, the KKS-Ru@AuNPs increased the lysosomal count and induced cell death. In vivo studies indicated that the concentration of KKS-Ru@AuNPs within tumor tissues reached 69.1 ± 26.6 ng Au/mg tissue, which is significantly greater than that observed using unmodified AuNPs. The tumor-targeting effect of KKS-Ru@AuNPs reduced the volume of orthotopic tumors by 84.6% and decreased the number of metastatic nodules in lungs by 41.7%. The observed multi-mechanism synergy exhibited by the KKS-Ru@AuNPs is attributable to the following: (1) RGDS-mediated active targeting, which enhances tumor accumulation, and (2) the spatiotemporal synergy between Ru complexes and photothermal effects that amplifies apoptotic signals. This study not only introduces a novel paradigm for the targeted delivery of Ru-based therapeutics but also establishes a theoretical foundation for developing multimodal nanoplatforms with simultaneous antitumor and antimetastatic capabilities.[9]

## Materials and Methods

All reagents and instruments employed in the study are listed in Tables S1 and S2. Furthermore, the detailed procedures for the synthesis and characterization of KKS and KKS-Ru, along with the operational protocols for DLS, TEM, and SEM analyses, as well as the experimental methods for live/dead cell staining and biological distribution assessed by ICP-MS, are fully described in the supporting documents.

### Synthesis of KKS and KKS-Ru

The reactive intermediates, 1-(quinolin-2-yl)-9*H*-pyrido[3,4-b]indole-3-carboxylic acid (KQ) and R($NO_2$)GD(OBzl)S-OBzl, were synthesized using a method described elsewhere.[31] Subsequently, as outlined in Figure 1, R($NO_2$)GD(OBzl)S-OBzl was sequentially condensed with Cbz-Lys(Boc)-COOH and KQ using EDC/HOBt-mediated amidation reaction to yield Cbz-K(KQ)-R($NO_2$)GD(OBzl)S-OBzl. The protecting groups were then removed by catalytic hydrogenolysis under mild conditions, yielding compound K(KQ)-RGDS, referred to as KKS ligand. Detailed experimental procedures and compound identifications are provided in the Supporting Information (Figure S1–S15).

Next, KKS ligand (85 mg, 0.1 mmol) was subjected to heating with 52 mg of $Ru(bpy)_2Cl_2$•$2H_2O$ (0.1 mmol) in ethanol at 60 °C for 48 hours. The resulting product was purified using C18 column chromatography, yielding 92 mg (71.1%) of the target compound [$(bpy)_2$Ru(II)(KKS)], designated as KKS-Ru complex, in the form of a purple–red solid powder (Purity: 90.43%; Q-TOF-MS (m/z): 1294.8997 $[M-H]^+$; Figure 2A). The $^1$H NMR spectrum in Figure 2B reveals that after Ru complexation, a distinctive bipyridine peak emerges while the peak related to the chiral carbon of RGDS exhibits a shift toward high field. The ultraviolet spectrum of KKS-Ru in Figure 2C shows a peak, which is characteristic of Ru-bipyridine, in the range of 400–500 nm. These results confirm the successful coordination of KKS with Ru.

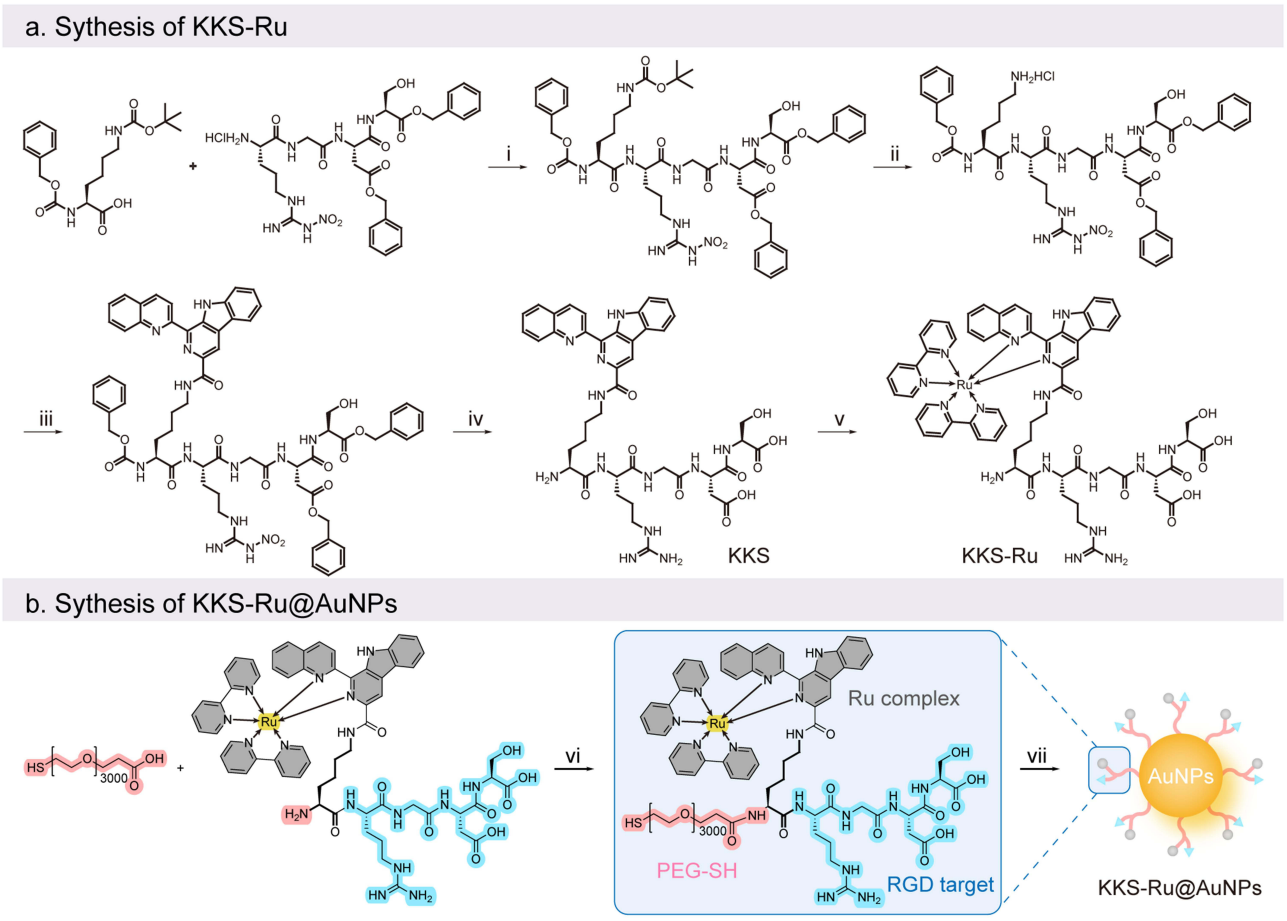


**Figure 1** Sythetic routes of (**a**) KKS-Ru and (**b**) KKS-Ru@AuNPs. (i) DCC, HOBt, THF, NMM; (ii) 4M HCl/EA; (iii) KQ, EDC, HOBt, THF, NMM; (iv) Pd/C, $H_2$, $CH_3OH$; (v) $(bpy)_2Ru(II)Cl_2 \cdot 2H_2O$, DMF/$H_2O$, pH 8.0, r.t., 24 hours; (vi) EDC, NHS; (vii) Stirring and incubating at r.t. for 4 hours, excess PEG-KKS-Ru was removed by centrifugation (11,000 rpm, 10 minutes) and washed three times with buffer.

## Preparation of KKS and KKS-Ru Nanoparticles

KKS and KKS-Ru nanoparticles were prepared using a conventional self-assembly technique.[32] Briefly, solid powders of KKS ligand and KKS-Ru complex were each dissolved in dimethyl sulfoxide (DMSO) to obtain stock solutions. Subsequently, ultrapure water, phosphate buffered saline, or normal saline were incrementally added under ultrasonic conditions for 30 minutes to induce nanoparticle formation. The final concentration of DMSO in the resulting solutions was maintained below 1% (v/v).

## Preparation of AuNPs and KKS-Ru@AuNPs

The KKS-Ru complex was conjugated with SH-$PEG_{3000}$-COOH via EDC/NHS-mediated coupling to obtain SH-$PEG_{3000}$-KKS-Ru (designated as PEG-KKS-Ru), which was purified by dialysis (MWCO: 3500 Da). This step activates the terminal carboxyl group of SH-$PEG_{3000}$-COOH by forming an amine-reactive NHS ester, allowing it to covalently bind to primary amine groups on the KKS-Ru complex through the formation of stable amide bonds.

Subsequently, KKS-Ru@AuNPs were synthesized by incubating PEG-KKS-Ru with AuNPs at various mass ratios, as detailed in Table S3. Control AuNPs were synthesized using SH-$PEG_{3000}$-COOH in place of SH-$PEG_{3000}$-KKS-Ru. The formation of KKS-Ru@AuNPs is primarily driven by the strong covalent coordination between the thiol (-SH) group at the distal end of the PEG spacer and the gold surface. This Au-S bond is one of the most stable interfacial linkages in nano-bioconjugation, providing robust anchoring of the PEG-KKS-Ru conjugate onto the AuNP core. Control AuNPs were synthesized using SH-$PEG_{3000}$-COOH in place of SH-$PEG_{3000}$-KKS-Ru.

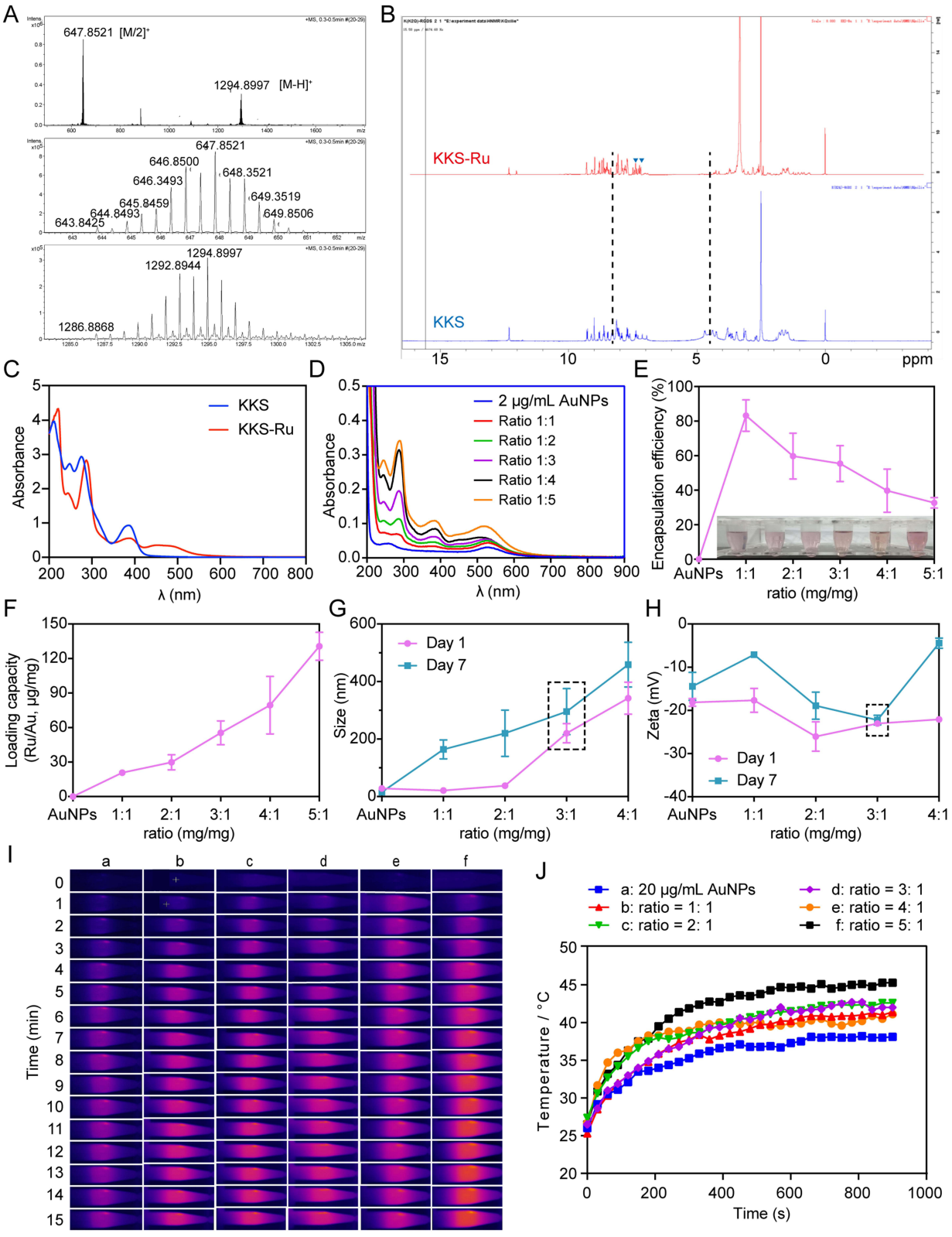


**Figure 2** Characterization of KKS-Ru and KKS-Ru@AuNPs. (**A**) FT-MS spectrum of KKS-Ru; (**B** and **C**) Changes in the $^{1}$H-NMR and UV-Vis spectra of KKS and KKS-Ru, confirming successful complexation; (**D**) UV-Vis data, (**E**) encapsulation efficiency, and (**F**) drug loading capacity (including photos of solutions) of KKS-Ru@AuNPs with increasing PEG-KKS-Ru: AuNPs mass ratio (1: 1 to 5: 1); (**G** and **H**) Nanoparticle size and zeta potential of KKS-Ru@AuNPs on day 1 and day 7 after preparation, with increasing KKS-Ru:AuNP mass ratios (1: 1 to 4: 1); (**I**) Thermal images and (**J**) corresponding temperature elevation profiles of KKS-Ru@AuNPs under 808 nm laser irradiation (1 W/cm², 0–15 minutes). Groups: (a) AuNPs; (b–f) KKS-Ru@AuNPs with increasing KKS-Ru:AuNP mass ratios from 1:1 to 5:1.


https://doi.org/10.2147/IJN.S547722

Specially, 1 mL of gold nanoparticles (size = 20 nm, concentration = 0.05 mg/mL) was centrifuged at 11,000 rpm for 10 minutes, the supernatant discarded, and the pellet washed twice with ultrapure water to remove citrate stabilizers and other impurities, thereby exposing the clean gold surface for efficient conjugation. The cleaned gold nanoparticles were resuspend in 950–750 μL of PBS or normal saline. PEG-KKS-Ru (1 mg/mL, 50–250 μL) was then added dropwise under stirring, and the mixture was incubated at room temperature for 4 hour to enable complete conjugation. During this incubation, the thiolated PEG-KKS-Ru ligands spontaneously assemble onto the AuNP surface via chemisorption, forming a stable, self-assembled monolayer that presents the KKS-Ru complexes outward into the solution. After incubation, unbound PEG-KKS-Ru was removed by centrifugation at 11,000 rpm for 10 min, followed by three washes with buffer to ensure the purification of the final conjugate and accurate quantification of loading efficiency. The final product KKS-Ru@AuNPs were stored at 4 °C. US-vis absorption spectroscopy confirmed successful surface modification of AuNPs with the Ru complex, while ICP-MS was employed to quantify drug loading and encapsulation efficiency.

## Photothermal Conversion Capacity

The photothermal conversion capacity of AuNPs and KKS-Ru@AuNPs was determined by monitoring temperature elevation using an infrared thermal imaging camera. Specifically, aqueous dispersions of AuNPs (20 μg/mL) and KKS-Ru@AuNPs at various KKS-Ru ratio (1:1, 2:1. 3:1, 4:1, 5:1) were irradiated with an 808 nm NIR laser at a power density of 1 W/cm² for 15 minutes, during which the temperature changes were recorded in real time. Additionally, the photothermal heating curves of KKS-Ru@AuNPs at different nanoparticle concentrations ($H_2O$ as control, 5, 10, and 20 μg/mL) were obtained under the same laser irradiation conditions (808 nm, 1 W/cm²) for 10 minutes. To evaluate photostability, the solution of KKS-Ru@AuNPs (20 μg/mL) was subjected to three consecutive laser on/off cycles, with temperature monitored throughout both irradiation and cooling periods.

## 3-(4,5-Dimethylthiazol-2-Yl)-2,5-Diphenyltetrazolium Bromide (MTT) Assay

The human non-small cell lung cancer cell line A549 were procured from Nanjing Kaiji Biotechnology (Nanjing, China) and cultured in RPMI-1640 medium containing 10% (v/v) FBS and 1% (v/v) penicillin-streptomycin. Cultures were maintained at 37 °C in a humidified 5% $CO_2$ atmosphere, with medium changes every two days.

For the cellular viability assay, A549 cells were seeded into 96-well plates at a density of a density of $4\times10^4$ cells/mL, with 100 μL of cell solution per well, and incubated overnight. Subsequently, 25 μL of KKS-Ru nanoparticles was added to each well to achieve final drug concentrations of 100, 50, 25, 12.5, 6.25, 3.125, and 1.5625 μM. Similarly, 25 μL of AuNPs or KKS-Ru@AuNPs was added to reach final Au concentrations of 100, 50, 25, 12.5, 6.25, 3.125, and 1.5625 μg/mL. After 24 hours of incubation, the cells were either irradiated (1 W/cm$^2$, 3 minutes) or not irradiated, followed by an additional culture period of 24 hours. Cell viability was then assessed using the MTT assay.

## Lysosomes Tracking for Flow Cytometry Analysis

A549 cells were cultured for 12 hours in six-well plates with KKS-Ru@AuNPs in the presence of 20 μg/mL Au. Subsequently, one experimental group was subjected to irradiation using an 808 nm laser operating at an intensity of 1 W/cm$^2$ for 3 minutes. Following an additional incubation for 12 hours, the cells were stained using lysosomal tracker (1:15000) for 30 minutes at 37 °C, and the nuclear DNA was stained with Hochest 33342 for 5 minutes. After washing with PBS, the stained cells were analyzed using a high-content image flow cytometry (Amnis® ImageStream Mk II, Luminex, Austin, TX, USA) and statistically analyzed by IDEAS 6.2.

## A549 Xenotransplantation Mouse Model

All animal procedures were approved by the Institutional Animal Care and Use Committee of Capital Medical University (NO. AEEI-2022-232), and complied with the guidelines of the protocol and the Regulations on Laboratory Animal Welfare issued by Chinese Ministry of Science and Technology. The research involved 30 female BALB/C nude mice, aged 8 weeks and weighing 18–20 g, purchased from Beijing Vital River Laboratory Animal Technology Co., Ltd. Prior to experimentation, the mice were raised under experimental environment at least 1 week.

Subsequently, the A549 tumor cells ($2\times10^6$ cells/mouse, 0.1 mL), in its logarithmic growth phase, were inoculated on the right dorsal side of BALB/C nude mice. Approximately 11 days later, when the tumor volume reached approximately 150 $mm^3$, the mice were randomly assigned to five groups, each comprising six mice (Table S4). The treatment regimen was continuously administered over a period of 14 days. During the treatment phase, tumor dimensions (length and width) were measured daily, and the tumor volume was calculated. On the 3rd, 7th, and 12th day of treatment, the tumor was irradiated using an 808 nm laser operating at an intensity of 1 $W/cm^2$ for 4 minutes. Following the final laser treatment, mice were weighed, and their blood samples were collected via orbital sinus puncture 24 hours later. Subsequently, the mice were euthanized by cervical dislocation. Blood samples were collected, with one portion used for routine hematological analysis and the remainder centrifuged at 3000 rpm for 10 minutes to obtain serum for biochemical assays. Tumors and major organs (heart, liver, spleen, lung, kidney, and brain) were excised. Pulmonary metastatic nodules were counted, and all tissues were stored at −80 °C for further analysis.

### Photoacoustic (PA) Imaging

Photoacoustic imaging was conducted to evaluate the tumor accumulation and distribution of nanoparticles in vivo. A549 tumor-bearing mice were intravenously injected with either AuNPs or KKS-Ru@AuNPs (20 μg/mL Au). Mice were then anesthetized with isoflurane and placed in the imaging chamber of a TomoWave LOIS-3D PA imaging system (USA). Three-dimensional PA imaging of the tumor site was performed at 0, 2, 6, 12, 24, and 48 hours post-injection using a wavelength of 660 nm optimized for AuNP absorption.

### Statistical Analysis

All experiments were conducted in triplicate, and data are expressed as mean ± standard deviation (SD). Statistical comparisons were performed using one-way ANOVA. * $p < 0.05$ and ** $p < 0.01$ were considered statistically significant.

## Results

### Characterization of KKS-Ru@AuNPs

The successful preparation of KKS-Ru@AuNPs were confirmed by ultraviolet-visible (UV-Vis) spectrophotometry (Figure 2D). With increasing PEG-KKS-Ru: AuNPs mass ratios, the characteristic absorption peak of AuNPs shifted from 525 nm to 515 nm, accompanied by enhanced absorption intensity. Additionally, a new characteristic absorption peak corresponding to Ru-bipyridine also appeared at ~380 nm. Concurrently, the solution color transitioned from purple to deep red (Figure 2E), indicating successful surface modification of AuNPs with KKS-Ru. Furthermore, the drug loading capacity and encapsulation efficiency were quantified via ICP-MS (Figure 2E and F). As the PEG-KKS-Ru: AuNPs mass ratio increased from 1: 1 to 5: 1, the Ru loading increased, while the encapsulation efficiency decreased, suggesting a saturation effect at higher ligand concentrations.

The optimal formulation ratio of KKS-Ru@AuNPs was evaluated using dynamic light scattering (DLS). As shown in Figure 2G, increasing the degree of PEG-KKS-Ru modification led to a progressive enlargement of the nanoparticles, which further increased over a seven-day storage period. Notably, the 3:1 PEG-KKS-Ru:AuNPs group showed the smallest size change which was measured ~200 nm on day 1 to ~300 nm on day 7, indicating superior stability. Figure 2H illustrates the variations in zeta potential at different PEG-KKS-Ru levels on day 1 and after seven days. Initially around −20 mV, the zeta potential became more negative with increasing PEG-KKS-Ru, reflecting its anionic nature. After storage for seven days, a general decline in the absolute zeta potential was observed, except in the 3:1 group, which showed minimal variation, further indicating its superior stability. Excessive PEG-KKS-Ru can lead to aggregation through steric hindrance and electrostatic interactions, while insufficient modification compromises stability and drug encapsulation efficiency. Overall, the 3:1 formulation achieved an optimal balance between drug loading and colloidal stability, making it suitable for subsequent investigations.

To assess the photothermal conversion capability of KKS-Ru@AuNPs, the temperature changes of nanoparticle dispersions were measured under 808 nm laser irradiation (1 $W/cm^2$) using an infrared thermal imaging device (Figure 2I

and J). The temperature of AuNPs increased by ~10 °C after 15 minutes of irradiation. In contrast, KKS-Ru@AuNPs exhibited a greater temperature rise of 16–20 °C, depending on the PEG-KKS-Ru ratio. Notably, the 3:1 formulation reached a temperature plateau within 10 minutes, demonstrating efficient and stable photothermal conversion. Compared with AuNPs, the enhanced performance of KKS-Ru@AuNPs enhancement may be attributed to the increased particle size, which has been linked to improved photothermal conversion efficiency. Furthermore, KKS-Ru modification precisely tuned the localized surface plasmon resonance (LSPR) properties of AuNPs, thereby enhancing their absorption efficiency under 808 nm laser irradiation. Such strong photothermal performance lays the foundation for PTT with chemotherapy, thereby enhancing the overall therapeutic efficacy of the nanoplatform.

## Nanoscale Properties

Transmission electron microscopy (TEM) and DLS technology were further employed to characterize the morphology and size of the nanoparticles. As shown in Figure 3A and B, KKS nanoparticles self-assembled into uniform spherical structures with an average diameter of ~281 nm, while KKS-Ru nanoparticles exhibited larger flower-like structures with an average size of ~1201 nm. In comparison, the unmodified AuNPs were well-dispersed nanospheres measuring ~25 nm. After surface modification, KKS-Ru@AuNPs appeared as irregular aggregates with an average core size of approximately 75 nm and visibly darker central regions, indicating the successful coating of AuNPs with KKS-Ru. Notably, DLS measurements revealed a larger hydrodynamic size of ~190 nm with a polydispersity index (PDI) of 0.20, suggesting a relatively uniform size distribution (Figure 3C). Such discrepancies are commonly observed since TEM only visualizes the dry physical core, whereas DLS measures the hydrodynamic diameter, which includes the hydrated shell and surface-bound molecules. Moreover, the irregular morphology of KKS-Ru@AuNPs may cause light scattering effects that further increase the apparent size measured by DLS.

To further evaluate colloidal stability of KKS-Ru@AuNPs under physiological conditions, the nanoparticles were incubated in serum-containing medium (10% FBS) for 0–24 hours. As shown in Figure S16, the particle size remained within 208–262 nm throughout the incubation period, with corresponding PDI values ranging from 0.23 to 0.41. The relatively narrow size distribution and stable PDI indicate that KKS-Ru@AuNPs exhibit low aggregation and maintain good colloidal stability under physiological conditions, which is essential for consistent performance and reliable in vivo therapeutic outcomes.

Interestingly, the KKS nanoparticles exhibited a positive zeta potential (Figure 3D), which is attributable to the exposure of guanidine groups on the nanoparticle surface following self-assembly. Upon complexation with Ru, the zeta potential shifted from positive to negative, presumably resulting from the incorporation of Ru-bipyridine, which alters the self-assembly structure and exposes the carboxyl groups on the surface of the nanoparticles. Notably, the absolute value of the zeta potential of KKS-Ru@AuNPs exceeded that of the AuNPs, suggesting that surface modification with PEG-KKS-Ru does not compromise, but may even enhance the colloidal stability of AuNPs.

## Photothermal Conversion Capacity

To precisely evaluate the contribution of the KKS-Ru molecular coating to photothermal performance, this study employed bare AuNPs with an identical core size (25 nm) as the control group. This approach effectively eliminates any influence of gold core size on the LSPR effect and photothermal conversion efficiency (PCE), thereby attributing observed performance differences primarily to the functional molecular modification. The solution of KKS-Ru@AuNPs was diluted to achieve solutions with Au concentrations of 5, 10, and 20 μg/mL. Temperature changes in the solution were monitored using water as a control. Figure 3E and F show that after 10 minutes of irradiation using an 808 nm laser operating at 1 W/cm², the temperatures of the solutions increase, with solutions having higher Au concentrations exhibiting a higher increase in temperature. The temperature increased over 46 °C for the KKS-Ru@AuNPs solution containing 20 μg/mL Au.

To evaluate the photothermal stability of KKS-Ru@AuNPs, the solution of KKS-Ru@AuNPs containing 20 μg/mL Au was subjected to irradiation using an 808 nm laser operating at for 15 minutes. Subsequently, the laser was turned off, and the solution was allowed to cool naturally to ambient temperature. The laser irradiation and cooling processes were repeated three times. As shown in Figure 3G, the temperature of the solution of KKS-Ru@AuNPs containing 20 μg/mL

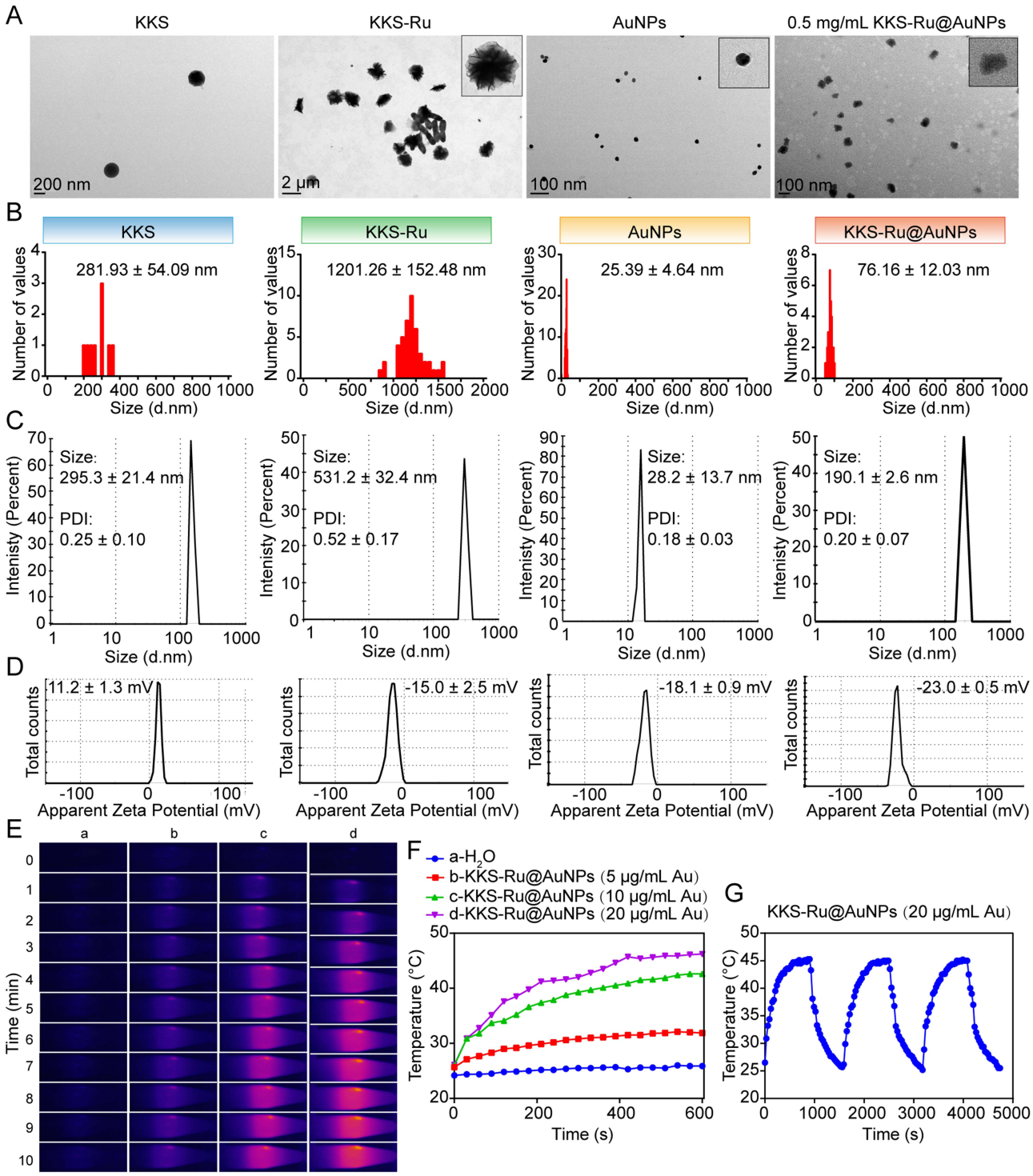


**Figure 3** Self-assembly characterization and photothermal properties of nanoparticles. (**A**) TEM images of KKS, KKS-Ru, AuNPs and KKS-Ru@AuNPs; (**B**) Particle size distribution determined from TEM images via ImageJ analysis; (**C**) Hydrodynamic diameters and (**D**) zeta potentials determined by dynamic light scattering; (**E**) Infrared thermal images and (**F**) corresponding temperature-time curves of KKS-Ru@AuNPs with varying Au concentrations under 808 nm laser irradiation at 1 W/cm$^2$ for 0–10 minutes, n = 3; (**G**) Photothermal stability of KKS-Ru@AuNPs containing 20 μg/mL Au over multiple cycles of 880 nm laser irradiation at 1 W/cm$^2$.

Au exceeds 45 °C in all three irradiation and cooling cycles, indicating photothermal stability of KKS-Ru@AuNPs. Simultaneously, we evaluated the release behavior of KKS-Ru@AuNPs under NIR laser irradiation at this concentration. The amount of Ru released with or without NIR exposure was quantitatively measured using ICP-MS. As shown in


https://doi.org/10.2147/IJN.S547722

Figure S17, laser irradiation significantly accelerated Ru release compared to the non-irradiated group, reaching a plateau within approximately 4 minutes with a release rate exceeding 94%. These results confirm that KKS-Ru@AuNPs exhibit a PTT-triggered drug release profile.

## Cell Viability

The cytotoxicity of KKS-Ru@AuNPs on tumor cells with and without laser irradiation was assessed using MTT assays and live/dead cell staining. As shown in Figure 4A, treatment with KKS-Ru@AuNPs at concentrations of 25, 50, and 100 μg/mL resulted in a marked decrease in cell viability upon 808 nm laser exposure. Similarly, unmodified AuNPs also exhibited reduced viability after laser irradiation, consistent with previous reports.[30] Notably, KKS-Ru@AuNPs combined with laser irradiation showed significantly greater cytotoxicity than AuNPs, KKS-Ru, or either treatment alone.

Live/dead staining further confirmed these findings (Figure 4B). Without laser irradiation, A549 cells treated with PBS (control group) and KKS-Ru@AuNPs (20 μg/mL Au), predominantly displayed green fluorescence, indicating viable cells. In contrast, cells incubated with KKS-Ru@AuNPs followed by 5 minutes of laser irradiation exhibited extensive red fluorescence, indicative of cell death. Collectively, these results demonstrate that KKS-Ru@AuNPs possess strong, laser-dependent cytotoxic activity, validating their potential for combined photothermal and chemotherapeutic treatment.

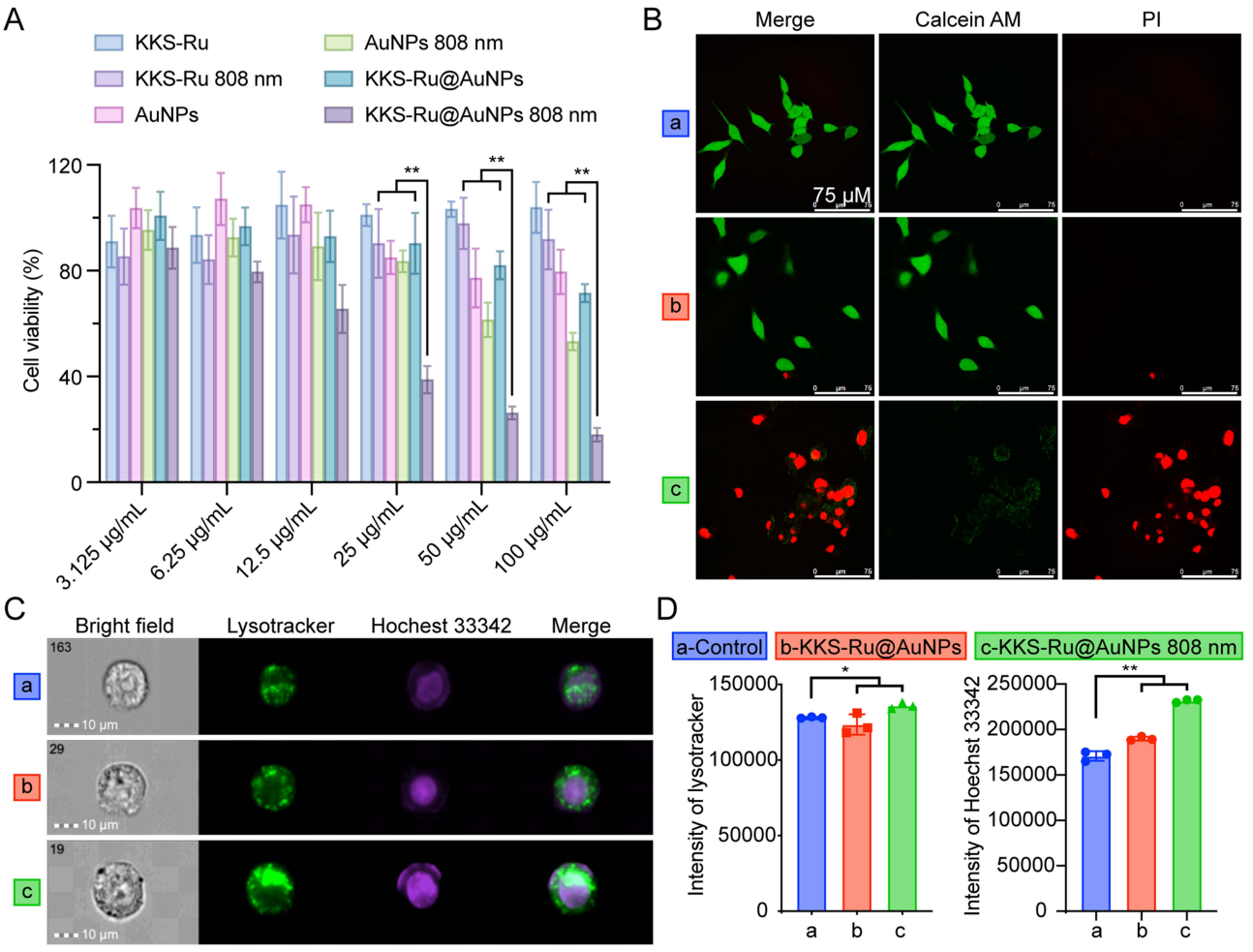


**Figure 4** In vitro photothermal activity of KKS-Ru@AuNPs. (**A**) Viability of A549 cells after 48 h of drug incubation, with or without 3 minutes of 808 nm laser irradiation at 1 W/cm$^2$; (**B**) Representative fluorescence images of Calcein AM/PI-stained A549 cells, showing live (green) and dead (red) populations after KKS-Ru@AuNPs treatment, with or without 3 minutes of 808 nm laser irradiation at 1 W/cm$^2$; (**C**) Representative flow cytometry images and (**D**) quantification of fluorescence intensity of lysosomal tracker/Hochest 33342 dual staining, n=3. * $P < 0.05$; ** $P < 0.01$.

## Lysosomal Tracking and Cell Death

According to the previous reports, Ru complexes induce cell death (apoptosis or necrosis) by compromising lysosomal stability.[31] Image flow cytometry was used to assess the fluorescence intensity of a lysosomal tracker and PI in KKS-Ru @AuNP-treated A549 cells. As shown in Figure 4C and D, cells exposed to KKS-Ru@AuNPs combined with 808 nm laser irradiation displayed a marked increase in lysosomal tracker and PI fluorescence compared to that in the control group. These results suggest that KKS-Ru@AuNPs induce tumor cell death by destabilizing lysosomes, consistent with a Ru-mediated cytotoxic mechanism.

## In vivo Tumor Suppression and Anti-Metastasis in A549 Tumor-Bearing Mouse Model

The photothermal therapeutic efficacy of KKS-Ru@AuNPs was assessed in an A549 xenograft mouse model. As depicted in Figure 5A, the experimental protocol involved initiating treatment when the tumor volume reached approximately 150 $cm^3$. The treatment included continuous administration of normal saline (NS), KKS-Ru, AuNPs, and KKS-Ru@AuNPs via the tail vein over a period of 14 days, coupled with irradiation using an 808 nm laser for 4 minutes on both the $3^{rd}$, $7^{th}$, and $12^{th}$ day of treatment. Temperature variations during laser exposure were recorded using a thermal imaging device. As shown in Figure 5B and C, after 4 minutes of laser irradiation, the maximum temperatures of local tumor in the NS, KKS-Ru, AuNPs, and KKS-Ru@AuNPs groups reached approximately 47 °C, 55 °C, 53 °C, and 57 °C, respectively. Furthermore, in the KKS-Ru@AuNPs group, temperatures surpassed 50 °C within the first minute of irradiation, indicating rapid heat generation and excellent in vivo photothermal performance.

Next, the variations in tumor volume and weight were assessed after various treatments. Figure 5D and E show that the tumor volume and weight in the treatment groups are reduced to a greater extent than those in the control group. Notably, the KKS-Ru@AuNPs + 808 nm laser group achieved a tumor inhibition rate of 84.6%, whereas the KKS-Ru + 808 nm, AuNPs + 808 nm, and KKS-Ru@AuNPs groups showed lower inhibition rates of 26.9%, 62.9%, and 30.3%, respectively. These results highlight the superior in vivo tumor inhibition efficacy of the KKS-Ru@AuNPs + 808 nm treatment, likely due to enhanced photothermal efficiency. Interestingly, tumor volume temporarily increased after each laser irradiation, which may be attributed to local tissue inflammation at elevated temperatures. This manifests macroscopically as a transient increase in tumor size, consistent with the common "pseudo-progression" phenomenon.[33]

After the final treatments, 24 hours later, the mice were euthanized under anesthesia, and their lung tissues (Figure 5F and G) were harvested for analysis. Figure 5F shows that the KKS-Ru or KKS-Ru@AuNPs + 808 nm laser treatment groups exhibit a significant reduction in the number of metastatic tumor nodules within the lungs. In contrast, the group treated with only KKS-Ru@AuNPs fails to impede lung tumor metastasis. This may be attributed to the fact that the KKS-Ru@AuNPs group without laser irradiation does not trigger the release of KKS-Ru, or alternatively, lacks the efficacy to eliminate the primary tumor.

## Body Distribution

To assess the in vivo distribution and metabolic processing of KKS-Ru@AuNPs, photoacoustic signals were recorded. This technique was employed owing to the strong near-infrared absorption and excellent photoacoustic properties of gold nanoparticles, which allow for deep-tissue, high-resolution imaging of their spatial distribution in living subjects. As shown in Figure 6A and B, both KKS-Ru@AuNPs and AuNPs rapidly accumulate at the tumor sites, persisting for over 24 hours, with subsequent excretion at 48 hours. Owing to the distinct photoacoustic imaging properties of AuNPs and KKS-Ru@AuNPs, a direct comparison of drug accumulation based on imaging signals alone is not feasible. ICP-MS was employed to quantitatively analyze the in vivo distribution of AuNPs and KKS-Ru@AuNPs within the tumor sites. After continuous administration of the desired nanoparticles for 14 days, the concentrations of Au in various internal organs were measured. Figure 6C shows that the concentrations of KKS-Ru@AuNPs are significantly higher than those of AuNPs in the tumor, lung, and kidney, whereas the concentrations of AuNPs and KKS-Ru@AuNPs in the liver and spleen are comparable.

Collectively, these results demonstrate that KKS-Ru@AuNPs achieve markedly higher in vivo absorption and targeting efficacy toward the tumor and lungs than AuNPs. This enhanced targeting likely underlies their superior ability

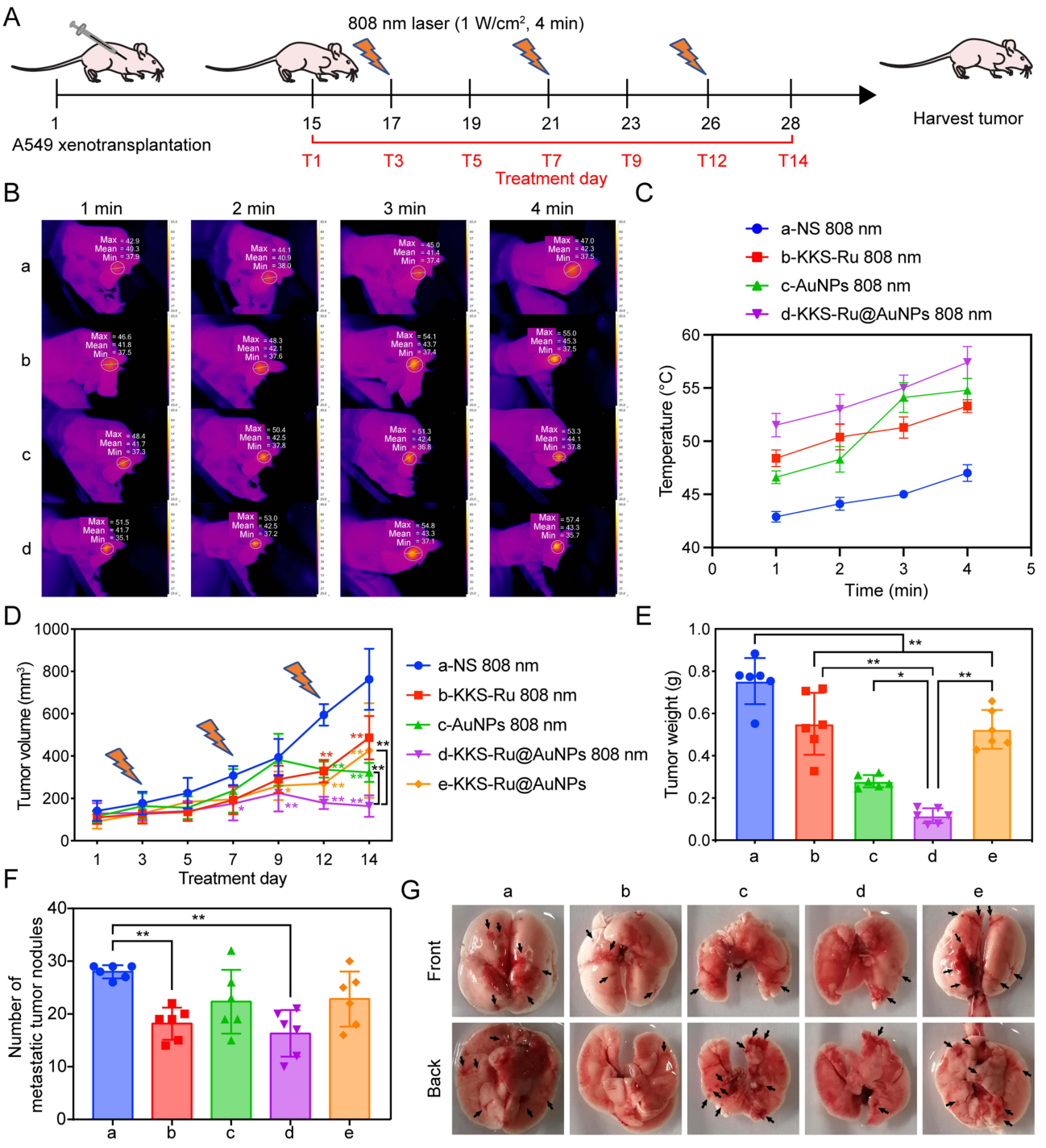


**Figure 5** In vivo photothermal therapeutic efficacy of KKS-Ru@AuNPs. (**A**) Schematic showing the treatment plan for A549 xenograft mice; (**B**) Representative infrared thermal images of tumor sites during 808 nm laser irradiation (1 W/cm$^2$, 4 minutes), n = 3; (**C**) Tumor temperature profiles recorded over the 4 minutes irradiation period; (**D**) Tumor volume growth curves in treated and control groups, n = 6; (**E**) Final tumor weights at treatment end point, n = 6; (**F**) Number of pulmonary metastatic tumor nodules, n = 6; (**G**) Representative photographs of the harvested lung tissues. * $P < 0.05$; ** $P < 0.01$.

to inhibit both primary tumor growth and pulmonary metastasis. Since laser irradiation was localized to the primary tumor, the reduction in lung metastases is primarily attributed to the synergistic effect of photothermal therapy and triggered chemotherapy at the primary site, effectively disrupting the metastatic cascade at its source. While systemic distribution, including lung accumulation, may provide an auxiliary chemotherapeutic benefit, this is considered a secondary and indirect mechanism.

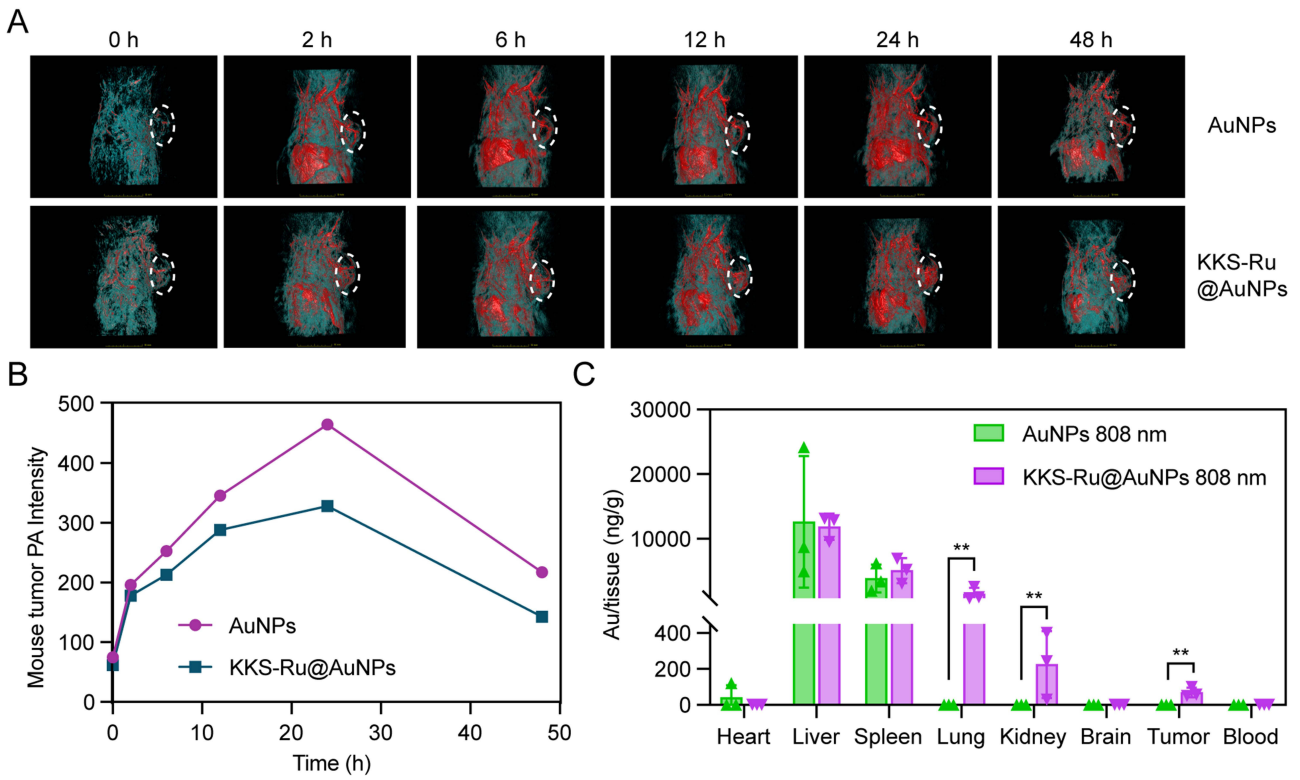


**Figure 6** In vivo biodistribution of KKS-Ru@AuNPs. (**A**) Representative photoacoustic images of A549 xenograft mice following intravenous injection of AuNPs or KKS-Ru @AuNPs. The dotted white circle represents the location of the tumor; (**B**) Quantified PA signal intensity in the tumor region at indicated time points; (**C**) Quantitative analysis of gold accumulation in major organs and tumor tissue from A549 xenograft mice treated with AuNPs + 808 nm or KKS-Ru@AuNPs + 808 nm, determined by ICP-MS and expressed as ng Au per g tissue. ** $P < 0.01$.

## Safety in vivo

To assess the in vivo safety of KKS-Ru@AuNPs as a nanomedicine, a comprehensive evaluation of body weight fluctuations of mice was conducted during the administration period. Additionally, the blood biochemical markers and routine hematological parameters of the treated mice were analyzed. As shown in Figure S18A, the body weights of the mice remained stable throughout the administration period. The blood biochemical markers, alanine aminotransferase (ALT) and aspartate aminotransferase (AST) exhibited no significant differences across the experimental groups (Figure S18B and C), suggesting that the continuous administration of KKS-Ru@AuNPs for 14 days does not induce any hepatic damage. No significant variations were observed in the renal function indicators, creatinine (Crea) and urea (Figure S18D and E), indicating the absence of overt nephrotoxicity after administration of KKS-Ru@AuNPs. Similarly, the white blood cell (WBC) and lymphocyte (Lym) counts remained unchanged (Figure S18F and G), suggesting that KKS-Ru @AuNPs can be used without causing any inflammatory responses, while stable red blood cell (RBC) and platelet (PLT) levels (Figure S18H and I) indicated no hematotoxicity. Additionally, H&E staining of the heart, liver, spleen, and kidney (Figure S19) showed no significant structural damage, further confirming the good systemic safety of KS-Ru for in vivo administration.

# Discussion

Compared to the previous reported Ru-based nanodrug KS-Ru,[31] KKS-Ru@AuNPs introduced an innovative therapeutic mechanism by incorporating photothermal therapy. Although both KS-Ru and KKS-Ru@AuNPs as nanodrugs exhibit a comparable efficiency in tumor accumulation facilitated by integrin targeting, KKS-Ru@AuNPs exhibits a markedly higher in situ tumor inhibition efficacy, increasing the tumor inhibition rate from 43% to 84.6%. The synergistic mechanism achieved after combining photothermal therapy with chemotherapy using KKS-Ru@AuNPs is possibly responsible for the observed excellent in situ tumor inhibition efficacy of KKS-Ru@AuNPs. The dual amplification


https://doi.org/10.2147/IJN.S547722

effects of Ru complexes and photothermal effects on lysosomal stress and apoptotic signaling can also be considered as contributing factors toward the observed in situ tumor inhibition efficacy of KKS-Ru@AuNPs. As compared to Au nanosphere-based NDDS,[30] KKS-Ru@AuNPs exhibit superior photothermal conversion capabilities. Moreover, KKS-Ru @AuNPs exhibit higher photothermal stability than that exhibited by Au nanorod-based NDDS. More importantly, in contrast to other reported Au-Ru hybrid systems,[21] our KKS-Ru@AuNPs are uniquely functionalized with the integrin-targeting RGD peptide, which represents a critical advancement that enables active tumor targeting and underlies the markedly enhanced therapeutic outcomes observed in this study. The multimodal design of KKS-Ru@AuNPs not only addresses the challenge of insufficient efficacy associated with Ru-based drugs but also establishes a theoretical foundation for developing smart nanodrugs with various capabilities, including precise delivery, in situ tumor eradication, and remote anti-metastasis.

The KKS-Ru@AuNPs exhibit the benefits of multi-mechanism synergistic therapy; however, the following issues require further research attention:

(1) Biocompatibility challenges: The accumulation of nanocarriers in the liver and kidney, with levels exceeding 171 times and 3.2 times that at the tumor site, respectively, poses a potential risk of long-term metabolic toxicity. Biocompatibility issues can be addressed by developing degradable Au-based nanocarriers, such as those utilizing glutathione-responsive Au–S bonding structures.[34] Future work will focus on designing such degradable systems to enhance metabolic clearance and reduce long-term retention in non-target organs.

(2) Limited targeting: The heterogeneity in integrin receptor expression reduces targeting efficiency toward tumors with low αvβ3 expression. Notably, the expression of RGD-binding integrins (eg, αvβ3) is highly variable across different tumor types, stages, and even within subregions of the same tumor, which may substantially limit the universal applicability of mono-targeted agents.[35] To improve clinical applicability, the development of multi-targeted aptamer systems, such as those utilizing RGD/ferrofolic acid dual-ligand modifications, is necessary.[36] Such strategies aim to overcome heterogeneity by simultaneously addressing multiple molecular targets, thereby broadening therapeutic coverage and enhancing targeting robustness.

(3) Insufficient elucidation of molecular mechanisms: The molecular switch that regulates the apoptotic pathway between the coordination of Ru complexes and photothermal effects should be clearly identified. Employing omics technologies is essential for systematically analyzing molecular mechanisms.[37]

(4) Translational potential: While the multi-component design of KKS-Ru@AuNPs introduces complexity, each element is crucial for its intended function: the Au core for PTT and carrier function, the Ru complex for chemotherapy, and the PEG-RGD moiety for stability and active targeting. This functional complexity is justified by a significantly enhanced therapeutic index. We acknowledge that scalability and reproducibility are key challenges for translation. However, the synthesis leverages well-established chemistries (eg, EDC/NHS coupling, Au-S bonding). Future efforts towards translation will focus on establishing robust Good Manufacturing Practice (GMP)-compliant processes, defining critical quality attributes (CQAs: eg, size, drug loading, targeting ligand density), and employing advanced analytical techniques for rigorous quality control throughout production.

## Conclusion

This study explored a peptide-linked Ru–Au nanocarrier system, KKS-Ru@AuNPs, for effectively utilizing the coupled effect of targeted chemotherapeutic properties of Ru complexes and photothermal therapeutic capabilities of Au nanospheres. KKS-Ru@AuNPs enabled achieving a synergistic effect characterized by tumor-specific accumulation, efficient in situ cytotoxicity, and anti-metastatic activity. The experimental results indicated that KKS-Ru@AuNPs, facilitated by the active targeting mechanism of the RGDS ligand, exhibit a higher drug accumulation at the tumor site compared to that exhibited by unmodified AuNPs. Furthermore, by exploiting the spatiotemporal synergy between apoptotic signals induced by Ru complexes and photothermal ablation, the KKS-Ru@AuNPs significantly inhibited in situ tumor growth, achieving a volume reduction of 84.6% and decreasing the number of metastatic lung nodules by 46%. The findings of this study underscore the potential of nanocarrier systems to optimize the functionality of metal complexes. Furthermore, this study provides a novel approach for developing synergistic multimechanistic antitumor strategies.

## Data Sharing Statement

Materials and protocols will be distributed to qualified scientific researchers for noncommercial and academic purposes. It is available from the corresponding author.

## Acknowledgments

The authors acknowledge the facilities supported by the Research and Development Laboratory of Innovative Drugs for Metabolic Diseases of the Capital Medical University (Beijing, China) and the Central Laboratory at Capital Medical University for experimental support.

## Author Contributions

All authors made a significant contribution to the work reported, whether that is in the conception, study design, execution, acquisition of data, analysis and interpretation, or in all these areas; took part in drafting, revising or critically reviewing the article; gave final approval of the version to be published; have agreed on the journal to which the article has been submitted; and agree to be accountable for all aspects of the work.

## Funding

This study is supported by the Natural Science Foundation of Beijing Municipality for Young Scholars (No. 2254070), the National Natural Science Foundation of China for Young Scholars (No. 22407094), and the National Natural Science Foundation Youth Science Fund Cultivation Project of Xuanwu Hospital of Capital Medical University (QNPY202401), the R&D Program of Beijing Municipal Education Commission (KM202410025024), and the Chinese Institutes for Medical Research, Beijing under the CIMR Organized Scientific Research Program (CX23YZ06).

## Disclosure

The authors declare no conflicts of interest related to this work.

## References

1. Lu Y, Zhu D, Le Q, Wang Y, Wang W. Ruthenium-based antitumor drugs and delivery systems from monotherapy to combination therapy. *Nanoscale*. 2022;14(44):16339–16375. doi:10.1039/D2NR02994D
2. Peter NMD, Simpson V, Casari I, Massi M, Falasca M. Metal-based antitumor compounds: beyond cisplatin. *Future Med Chem*. 2018;11 (2):119–135.
3. Zeng X, Wang Y, Han J, et al. Fighting against Drug-Resistant Tumors using a Dual-Responsive Pt(IV)/Ru(II) Bimetallic Polymer. *Adv Mater*. 2020;32(43):e2004766. doi:10.1002/adma.202004766
4. Bonnet S. Ruthenium-Based Photoactivated Chemotherapy. *J Am Chem Soc*. 2023;145(43):23397–23415. doi:10.1021/jacs.3c01135
5. Chen Q, He L, Li X, Xu L, Chen T. Ruthenium complexes boost NK cell immunotherapy via sensitizing triple-negative breast cancer and shaping immuno-microenvironment. *Biomaterials*. 2022;281:121371. doi:10.1016/j.biomaterials.2022.121371
6. Das U, Basu U, Paira P. Recent trends in the design and delivery strategies of ruthenium complexes for breast cancer therapy. *Dalton Trans*. 2024;53(36):15113–15157. doi:10.1039/d4dt01482k
7. Pena Q, Wang A, Zaremba O, et al. Metallodrugs in cancer nanomedicine. *Chem Soc Rev*. 2022;51(7):2544–2582. doi:10.1039/d1cs00468a
8. Lee SY, Kim CY, Nam TG. Ruthenium Complexes as Anticancer Agents: a Brief History and Perspectives. *Drug Des Devel Ther*. 2020;14:5375–5392. doi:10.2147/DDDT.S275007
9. Zhang L, Wang P, Zhou XQ, et al. Cyclic Ruthenium-Peptide Conjugates as Integrin-Targeting Phototherapeutic Prodrugs for the Treatment of Brain Tumors. *J Am Chem Soc*. 2023;145(27):14963–14980. doi:10.1021/jacs.3c04855
10. Kulkarni GS, Lilge L, Nesbitt M, Dumoulin-White RJ, Mandel A, Jewett MAS. A Phase 1b Clinical Study of Intravesical Photodynamic Therapy in Patients with Bacillus Calmette-Guerin-unresponsive Non-muscle-invasive Bladder Cancer. *Eur Urol Open Sci*. 2022;41:105–111. doi:10.1016/j.euros.2022.04.015
11. Papish ET, Oladipupo OE. Factors that influence singlet oxygen formation vs. ligand substitution for light-activated ruthenium anticancer compounds. *Curr Opin Chem Biol*. 2022;68:102143. doi:10.1016/j.cbpa.2022.102143
12. Huang L, Zhao S, Fang F, Xu T, Lan M, Zhang J. Advances and perspectives in carrier-free nanodrugs for cancer chemo-monotherapy and combination therapy. *Biomaterials*. 2021;268:120557. doi:10.1016/j.biomaterials.2020.120557
13. Arlt S, Petkovic V, Ludwig G, et al. Arene Ruthenium(II) Complexes Bearing the kappa-P or kappa-P,kappa-S Ph(2)P(CH(2))(3)SPh Ligand. *Molecules*. 2021;26(7):1860. doi:10.3390/molecules26071860
14. Bu S, Jiang G, Jiang G, et al. Antibacterial activity of ruthenium polypyridyl complexes against Staphylococcus aureus and biofilms. *J Biol Inorg Chem*. 2020;25(5):747–757. doi:10.1007/s00775-020-01797-w
15. Chen BC, Lu JJ, Jiang N, Ma XR, Li RT, Ye RR. Synthesis, characterization and antitumor mechanism investigation of ruthenium(II) polypyridyl complexes with artesunate moiety. *J Biol Inorg Chem*. 2021;26(8):909–918. doi:10.1007/s00775-021-01901-8

16. Golbaghi G, Castonguay A. Rationally Designed Ruthenium Complexes for Breast Cancer Therapy. *Molecules*. 2020;25(2):265. doi:10.3390/molecules25020265
17. Li Y, Huang F, Stang PJ, Yin S. Supramolecular Coordination Complexes for Synergistic Cancer Therapy. *Acc Chem Res*. 2024;57(8):1174–1187. doi:10.1021/acs.accounts.4c00031
18. Zhang J, Ma W, Yang B, et al. Biomimetic Metallacage Nanoparticles with Aggregation-Induced Emission for NIR-II Fluorescence Imaging-Guided Synergistic Immuno-Phototherapy of Tumors. *ACS Appl Mater Interfaces*. 2024;16(50):69028–69044. doi:10.1021/acsami.4c17413
19. Xu D, Li Y, Yin S, Huang F. Strategies to address key challenges of metallacycle/metallacage-based supramolecular coordination complexes in biomedical applications. *Chem Soc Rev*. 2024;53(6):3167–3204. doi:10.1039/d3cs00926b
20. Lin X, Chen F, Yu X, et al. Phenylthiol-BODIPY-based supramolecular metallacycles for synergistic tumor chemo-photodynamic therapy. *Proc Natl Acad Sci U S A*. 2022;119(29):e2203994119. doi:10.1073/pnas.2203994119
21. Huang X, Sun X, Wang W, et al. Nanoscale metal-organic frameworks for tumor phototherapy. *J Mater Chem B*. 2021;9(18):3756–3777. doi:10.1039/D1TB00349F
22. Irvine DJ, Dane EL. Enhancing cancer immunotherapy with nanomedicine. *Nat Rev Immunol*. 2020;20(5):321–334. doi:10.1038/s41577-019-0269-6
23. Karaosmanoglu S, Zhou M, Shi B, Zhang X, Williams GR, Chen X. Carrier-free nanodrugs for safe and effective cancer treatment. *J Control Release*. 2021;329:805–832. doi:10.1016/j.jconrel.2020.10.014
24. Alamzadeh Z, Beik J, Mirrahimi M, et al. Gold nanoparticles promote a multimodal synergistic cancer therapy strategy by co-delivery of thermo-chemo-radio therapy. *Eur J Pharm Sci*. 2020;145:105235. doi:10.1016/j.ejps.2020.105235
25. Gopalakrishnan D, Saravanan S, Merckx R, et al. N,N-Ru(II)-p-cymene-poly(N-vinylpyrrolidone) surface functionalized gold nanoparticles: from organoruthenium complex to nanomaterial for antiproliferative activity. *Dalton Trans*. 2021;50(23):8232–8242. doi:10.1039/D1DT00694K
26. Alavi M, Hamidi M. Passive and active targeting in cancer therapy by liposomes and lipid nanoparticles. *Drug Metab Pers Ther*. 2019;34(1):1.
27. Zhao Z, Zhang X, Li CE, Chen T. Designing luminescent ruthenium prodrug for precise cancer therapy and rapid clinical diagnosis. *Biomaterials*. 2019;192:579–589. doi:10.1016/j.biomaterials.2018.12.002
28. Gonzalez JLC, Casillas PEG, Gonzalez CC. Gold Nanoparticles as Drug Carriers: the Role of Silica and PEG as Surface Coatings in Optimizing Drug Loading. *Micromachines*. 2023;14(2):451. doi:10.3390/mi14020451
29. Adhikari S, Nath P, Das A, et al. A review on metal complexes and its anti-cancer activities: recent updates from in vivo studies. *Biomed Pharmacother*. 2024;171:116211. doi:10.1016/j.biopha.2024.116211
30. Lu Y, Peng Z, Zhu D, et al. RGD Peptide and PAD4 Inhibitor-Loaded Gold Nanorods for Chemo-Photothermal Combined Therapy to Inhibit Tumor Growth, Prevent Lung Metastasis and Improve Biosafety. *Int J Nanomed*. 2021;16:5565–5580. doi:10.2147/IJN.S319210
31. Lu Y, Zhu D, Hu B, et al. pH-Responsive, Self-Assembled Ruthenium Nanodrug: dual Impact on Lysosomes and DNA for Synergistic Chemotherapy and Immunogenic Cell Death. *Small*. 2024;20(24):e2310636. doi:10.1002/smll.202310636
32. Cui C, Wang C, Fu Q, et al. A generic self-assembly approach towards phototheranostics for NIR-II fluorescence imaging and phototherapy. *Acta Biomater*. 2022;140:601–609. doi:10.1016/j.actbio.2021.11.023
33. Ma Y, Wang Q, Dong Q, Zhan L, Zhang J. How to differentiate pseudoprogression from true progression in cancer patients treated with immunotherapy. *Am J Cancer Res*. 2019;9(8):1546–1553.
34. Layachi M, Treizebre A, Hay L, et al. Novel opto-fluidic drug delivery system for efficient cellular transfection. *J Nanobiotechnology*. 2023;21(1):43. doi:10.1186/s12951-023-01797-3
35. Voorzanger-Rousselot N, Garnero P. Biochemical markers in oncology. Part I: molecular basis. Part II: clinical uses. *Cancer Treat Rev*. 2007;33(3):230–283. doi:10.1016/j.ctrv.2007.01.008
36. Cao Y, Wu T, Zhang K, et al. Engineered Exosome-Mediated Near-Infrared-II Region V(2)C Quantum Dot Delivery for Nucleus-Target Low-Temperature Photothermal Therapy. *ACS Nano*. 2019;13(2):1499–1510. doi:10.1021/acsnano.8b07224
37. Zhang T, Lei T, Yan R, et al. Systemic and single cell level responses to 1 nm size biomaterials demonstrate distinct biological effects revealed by multi-omics atlas. *Bioact Mater*. 2022;18:199–212. doi:10.1016/j.bioactmat.2022.03.026